Journal of Power Sources 196 (2011) 10518–10525

Contents lists available at ScienceDirect

Journal of Power Sources

journal homepage: www.elsevier.com/locate/jpowsour

Mesoporous F-doped ZnO prism arrays with significantly enhanced photovoltaic performance for dye-sensitized solar cells

Lijuan Luo[a], Wei Tao[a], Xiaoyan Hu[a], Ting Xiao[a], Bojun Heng[a], Wei Huang[a], Heng Wang[b], Hongwei Han[b], Qike Jiang[c], Jianbo Wang[c], Yiwen Tang[a,*]

[a] Institute of Nano-science and Technology, Central China Normal University, Wuhan 430079, China
[b] Michael Grätzel Center for Mesoscopic Solar Cells, Wuhan National Laboratory for Optoelectronics, Huazhong University of Science and Technology, Wuhan 430074, China
[c] Department of Physics and Key Laboratory of Acoustic and Photonic Materials and Devices of Ministry of Education, Wuhan University, Wuhan 430072, China

ARTICLE INFO

Article history:
Received 8 March 2011
Received in revised form 23 June 2011
Accepted 2 August 2011
Available online 22 August 2011

Keywords:
F-doped ZnO
Prism array
Mesoporous
Dye-sensitized solar cell
Photovoltaic

ABSTRACT

A photoanode with a mesoporous F-doped ZnO prism array (F-ZnO PA) is prepared on an F-SnO_2 (FTO) glass substrate and its application in a dye-sensitized solar cell (DSSC) is investigated. A superstructure of mesoporous F-ZnO PA is obtained by thermal treatment of ZnF(OH) PA precursor, which has been previously grown directly onto the FTO substrate via chemical bath deposition. The structure and morphology of the films are characterized by X-ray powder diffraction (XRD), scanning electron microscopy (SEM), transmission electron microscopy (TEM) and TEM-EDS elemental mapping. The ZnO prisms are homogenously doped by F and composed of oriented nanograins and nanopores. Owing to the higher surface area and stronger light scattering, as well as longer electron lifetime and lower charge-transfer resistance, an electrical energy conversion efficiency (η) of 3.43% is achieved for a DSSC containing a 5 μm thick mesoporous F-ZnO PA photoanode, which is much higher than that for a similar cell based on a ZnO nanorod photoanode. The knowledge acquired in this work is important for the design of efficient photoanode materials for DSSCs.

1. Introduction

As a promising candidate for the photoanode of dye-sensitized solar cells (DSSCs), nanostructured ZnO with different morphologies has attracted much attention over the last few years due to the similarity in energy band gap and electron-injection process of ZnO to those of TiO_2. More importantly, its much higher carrier mobility is more favorable for the collection of photoinduced electrons [1,2]. It is well known that one-dimensional (1D) ZnO nanostructures exhibit excellent device performance in optoelectronic light-emitting diodes and photoanodes for DSSC applications [3–5]. Recent studies on ZnO DSSCs have mostly focused on photoanodes with 1D nanostructures, such as nanowires or nanotubes, in view of their low trap density and the direct path to the current collecting electrode that can speed up charge migration without adversely affecting recombination [6–8]. However, the overall solar-to-electric energy-conversion efficiency is limited by insufficient surface area of the nanowire/nanotube array or poor light-scattering capabilities. Until now, no more than 2.4% power conversion efficiency has been reported for ZnO nanowire or nanotube array photoanodes [9,10]. One effective approach to increase the surface area of the array is to produce mesopores within 1D ZnO arrays, as has been demonstrated for 2D ZnO nanoplates [11]. On the other hand, ZnO films with hierarchical structure can offer both sufficient internal surface area for dye-adsorption and large particles for effective light-scattering [12,13]. In addition to high porosity and specific surface area, cationic or anionic doping with an alternate element has been found to be a very effective way to enhance the efficiency of DSSCs [14,15].

Many research groups have demonstrated that thermal decomposition of precursors, e.g., zinc oxalate, zinc hydroxide, or zinc carbonate, can successfully lead to construction of complex ZnO nanoarchitectures [16–18]. Very recently, Xu et al. [19] have reported the synthesis of mesoporous rhombus-like ZnO nanorod (NR) arrays via a two-step approach. The route first involved electrodeposition of vertically aligned rhombic ZnFOH nanorod arrays, followed by pyrolysis of the ZnFOH intermediate into ZnO with the same morphology. However, their resultant ZnO products were polycrystalline in nature, resulting from the polycrystalline ZnFOH nanorod precursor, which may limit the overall solar-to-electrical energy-conversion efficiency of the corresponding ZnO-based DSSCs. Wet chemical routes are useful for "electroless deposition" processes, which do not require complex equipment or electricity [20]. In the present study, we have attempted to fabricate single-crystalline ZnF(OH) prism arrays on an FTO glass substrate in a Zn-NH_4F solution via wet chemical routes.

* Corresponding author. Tel.: +86 27 67867947; fax: +86 27 67861185.
E-mail address: ywtang@phy.ccnu.edu.cn (Y. Tang).

0378-7753/$ – see front matter © 2011 Elsevier B.V. All rights reserved.
doi:10.1016/j.jpowsour.2011.08.011

A superstructure of mesoporous F doped ZnO prism array (F-ZnO PA) with highly oriented crystal grains has been obtained by thermal transformation of ZnF(OH) prism array precursors in air. Several design benefits can be envisaged for such an F-ZnO photoanode. First, the mesoporous prism structure provides a large internal surface area for dye molecule adsorption, which is significant for a DSSC. Second, because of its aligned single-crystalline-like structure, the F-ZnO prism, despite its nanopores, is almost as effective as vertically aligned NR in reducing the number of electron-hopping junctions in the film. Conventional porous nanoparticle films, in contrast, have significant resistance from these junctions. Third, the submicrometer-sized prisms act as light scatterers to enhance the light harvesting. In our preliminary experiments, we have achieved a maximum conversion efficiency of 3.43% using a 5 μm thick mesoporous F-ZnO PA as the photoanode in a DSSC under 90 mW cm^{-2} illumination; this is much more efficient than a similar DSSC based on a ZnO NR film photoanode.

2. Experimental

2.1. Preparation of hierarchically mesoporous F-ZnO PA film

F-ZnO PA films were prepared using a two-step experimental procedure, which comprised an initial low temperature chemical bath process and a annealing following. Before chemical bathing, F-doped SnO_2 glass substrates (FTO, 10–15 Ω sq^{-1}, Asahi Company) were ultrasonically cleaned in water and ethanol before being dip-coated to give a thin ZnO sol layer, and annealed at 500 °C for 30 min to obtain a ZnO seed film. The chemical bath solution was made by dissolving 0.05 M $Zn(NO_3)_2$ and 0.2 M NH_4F in deionized water. The seeded substrate was placed vertically into a beaker with the reverse side against the beaker wall. The chemical bath reaction was carried out at 70 °C for 1 h; prism arrays of ZnF(OH) were obtained on the FTO substrate. Then the ZnF(OH) array films were cleaned under running water and dried at room temperature, followed by annealing in a tube furnace at 500 °C for 1 h to yield F-ZnO PA. The annealing treatment must be carried out in a tube furnace in a highly efficient fume hood, because the HF produced by the thermal decomposition of ZnF(OH) is highly poisonous.

For comparison with the F-ZnO, ZnO NR films were fabricated as described in our previous work [21].

2.2. Characterization

The crystallinity and phase purity of the product were examined by a Bruker D8 Advance X-ray diffractometer (XRD) with monochromatized Cu Kα radiation (λ = 1.5418 Å), recorded with 2θ ranging from 10° to 80°. The morphology and structure of the as-synthesized product were characterized using a JEOL JEM-2010 transmission electron microscope (TEM) operating at 200 kV and a JEOL JSM-6700F scanning electron microscope (SEM). Energy dispersive spectroscopy (EDS) elemental mapping measurements were recorded using JEM2100F high-resolution transmission electron microscope (HRTEM) with energy filter (GIF Tridium). The stoichiometry of the products was examined by X-ray photoelectron spectroscopy (XPS) using a VG Multilab 2000X spectrometer with a standard and monochromatic source (Al Kα) operated at 150 W. In the XPS measurements, all binding-energies were referenced to the main C_{1s} peak at 284.6 eV. Thermal analysis (TG–DTA) was carried out with a Netzsch Sta 449c thermal analyzer at a heating rate of 10 °C min^{-1}.

2.3. DSSC fabrication and performance measurements

Prior to solar cell testing, the F-ZnO PA and ZnO NR obtained were heated at 80 °C for 30 min and then immersed in a 0.3 mM ethanolic solution of the ruthenium complex cis-bis(2,2′-bipyridyl-4,4′-dicarboxylato)-ruthenium(II)-bis-tetrabutylammonium (commercially known as N719 dye) overnight at room temperature. Then the sensitized films were rinsed with ethanol to remove excess dye from the surface and air-dried at room temperature.

The sensitized electrode was incorporated into a typical cell; namely, a Pt counter electrode was placed over the dye-sensitized photoanode, and then the photoelectrochemical properties of the DSSC were measured. The electrolyte solution, which consisted of 0.60 M 1-butyl-3-methylimidazolium iodide, 0.03 M I_2, and 0.50 M tertbutylpyridine in acetonitrile/valeronitrile (85:15), was injected into the space between the photoanode and the counter electrode. The active area of the resultant cell exposed to light was 0.2 cm^2. The photoelectrochemical tests of the DSSCs were performed under one sun conditions using a solar light simulator (Oriel, 69911, AM 1.5 globe). The photocurrent–voltage characteristics were measured using a Princeton Applied Research Model 263A Potentiostat/Galvanostat. The incident photo-to-current conversion efficiency (IPCE) was measured with a Dual-Channel Optical Meter Model 2931-C (Newport). To quantify the dye content of the ZnO electrodes, the dye was desorbed into 0.2 mM NaOH solution [22], and then the absorption spectrum of the desorbed dye solution was measured using a UV-vis spectrophotometer (Perkin Elmer Lambda35). The electrochemical impedance spectra (EIS) measurements in this study were carried out by applying bias of the open circuit voltage V_{OC} in a frequency range from 0.1 Hz to 100 kHz with an ac amplitude of 10 mV. The photocurrent–voltage characteristics and EIS measurements of all the DSSCs were performed under the irradiation light intensity of 90 mW cm^{-2}.

3. Results and discussion

3.1. Structure and morphology of ZnF(OH) prism arrays

The intermediate product, ZnF(OH) column array with a prism structure, was prepared by chemical bath deposition – placing a seeded FTO substrate into a mixed solution consisting of 0.05 M $Zn(NO_3)_2$ and 0.2 M NH_4F at 70 °C for 1 h. X-ray diffraction (XRD) measurements show that the intermediate product obtained is orthorhombic ZnF(OH) (Fig. 1a, JCPDS file No. 74-1816) with lattice constants of a = 10.13 Å, c = 3.12 Å. No impurity peaks were detected, indicating the high purity of the obtained ZnF(OH) array film. The SEM image in Fig. 1b shows an overview of the as-prepared ZnF(OH). The product consists of a large, well-aligned, prism-like nanostructure, which uniformly covers the entire surface of the FTO substrate. The cross-section view in Fig. 1c shows that these ZnF(OH) prisms are aligned in a dense array approximately perpendicular to the substrate surface, and have large gaps between them. The surface of each prism is very smooth. The prisms range from 100 nm to 1.5 μm across and the film thickness is 5 μm, which is approximately the average prism length (Fig. 1c). The surface of the ZnF(OH) column precursors is also found to be smooth in the transmission electron microscope (TEM) image of Fig. 1d. The corresponding selected-area electron diffraction (SAED) pattern of the ZnF(OH) prism in the inset of Fig. 1d exhibits two sets of diffraction spots, indicating that the prisms possess single-crystalline structure.

3.2. Structure and morphology of the mesoporous F-ZnO PA

Thermo-gravimetric/differential thermal analysis (TG/DTA) was used to follow the heat treatment process of the as-prepared ZnF(OH) in air. The DTA curve in Fig. S1 in the Supporting Information shows that the thermal decomposition of the precursor is an endothermic process, with only one obvious endothermic peak

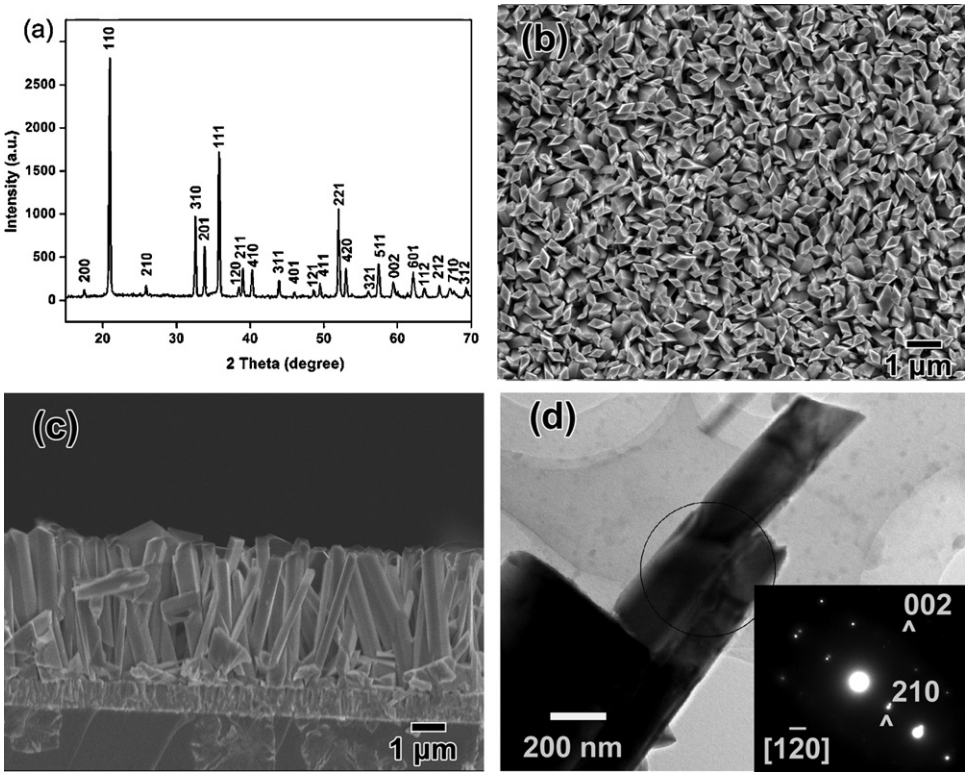

Fig. 1. (a) XRD pattern, (b) SEM, (c) SEM cross-section and (d) TEM image of the ZnF(OH) precursors.

at about 403 °C. The total weight loss of 13.8% in the TG curve is ascribed to the release of HF during decomposition of the ZnF(OH) according to Eq. (1).

$$Zn(OH)F \rightarrow ZnO + HF\uparrow \quad (1)$$

After heat treatment of the ZnF(OH) prism array at 500 °C for 1 h in air, XRD shows that the final product is single-phase hexagonal wurtzite ZnO (Fig. 2a, JCPDS file No. 74-1816), which is in agreement with the previous report. However, XPS results (see Fig. S2 in the Supporting Information) show that the annealed ZnO film contains a small amount of F (1.38 atom%). A detailed chemical analysis was carried out using EDX elemental mapping. Fig. 2b shows a typical TEM image of a prism scratched from an annealed film and its corresponding EDS elemental maps are shown in Fig. 2c–e. The Zn, O, and F elemental maps have the same spatial distribution as the TEM image. This indicates quite a uniform distribution of elements in the synthesized products, and demonstrates that the ZnO prisms are homogenously doped with F. The UV absorbance edge (Fig. S3 in the supporting information) of the F-ZnO film is close to 425 nm (E_g = 3.08 eV) in the visible region, which is a large shift toward the lower energy side (red-shift) relative to the pure ZnO (about 380 nm). This result is accordance with Vijayakumar's reports about the optical absorption changes of F-doped ZnO films [23]. The typical green emission PL spectra of F-ZnO PA and ZnO NR array films with the same thickness of 3 μm (Fig. S4 in the supporting information) were analyzed. The deep-level emission in the green band is generally related to variation in the intrinsic defects in ZnO films, such as zinc vacancies (V_{Zn}), interstitial zincs (Zn_i) and oxygen vacancies (V_o) [24,25]. In our case, the green emission peak intensity of F-ZnO is much weaker than that of ZnO NR. The significant difference in the intensity between F-ZnO PA and ZnO NR is ascribed to the low density of V_o resulting from substitution of doped F for O in F-ZnO [26].

Overall SEM observations (Fig. 3a) show that the F-ZnO prisms have similar shape and size distributions to the intermediate ZnF(OH) prisms, implying the prism-like conformation of the precursor is maintained. However, in contrast to the intermediate ZnF(OH), the F-ZnO prism contains numerous nanocrystals (about 20 nm) and mesopores, which are visible on the top surfaces of the prisms as shown in the high-magnification SEM image (the inset of Fig. 3a) of an individual prism top end. The cross-section image (Fig. 3b) also shows that the prism morphology of F-ZnO has not been deformed during the pyrolysis of ZnF(OH). The magnified SEM image (Fig. 3c) for the region marked as B in Fig. 3b clearly shows uniform nanoporous channel morphology at the side of the prism, resulting from the release of HF produced during the pyrolysis procedure. To explore the inner morphology of the F-ZnO prism, we took an SEM image of the region marked C (Fig. 3b) in which the F-ZnO prisms were broken. It can be distinctly seen from Fig. 3d that there are many pores located along each prism.

The mesoporous F-ZnO prisms were subjected to further investigations by TEM, HRTEM, and SAED. The TEM image in Fig. 4a reveals unambiguously that there are numerous mesopores inside the prism. The corresponding SAED pattern of the prism is composed of isolated symmetrical spots (inset of Fig. 4a), meaning that all the nanoparticles in the prism possess almost the same crystallographic orientation. The HRTEM of an individual F-ZnO prism is shown in Fig. 4b, together with the enlarged image (Fig. 4c) of the area marked by frames in Fig. 4b. Obvious porous structure could be observed in Fig. 4b and the typical size of the mesopores is about 10 nm. The HRTEM image of the single prism exhibits clear and coherent lattice fringes running through the whole porous prism. Slight misorientations between nanoparticles, as well as defects (such as dislocations), can also be observed; these are responsible for the arc texture of the diffraction spots in the SAED pattern corresponding to the imperfectly oriented attachment of the nanoparticles. The measured lattice spacing from HRTEM is almost the same as that for ZnO and the planes with much finer spacing can be attributed to (1 0 $\bar{1}$ 1) and (0 $\bar{1}$ 1 1) characteristic of hexagonal ZnO (Fig. 4c). The inset in Fig. 4c is the

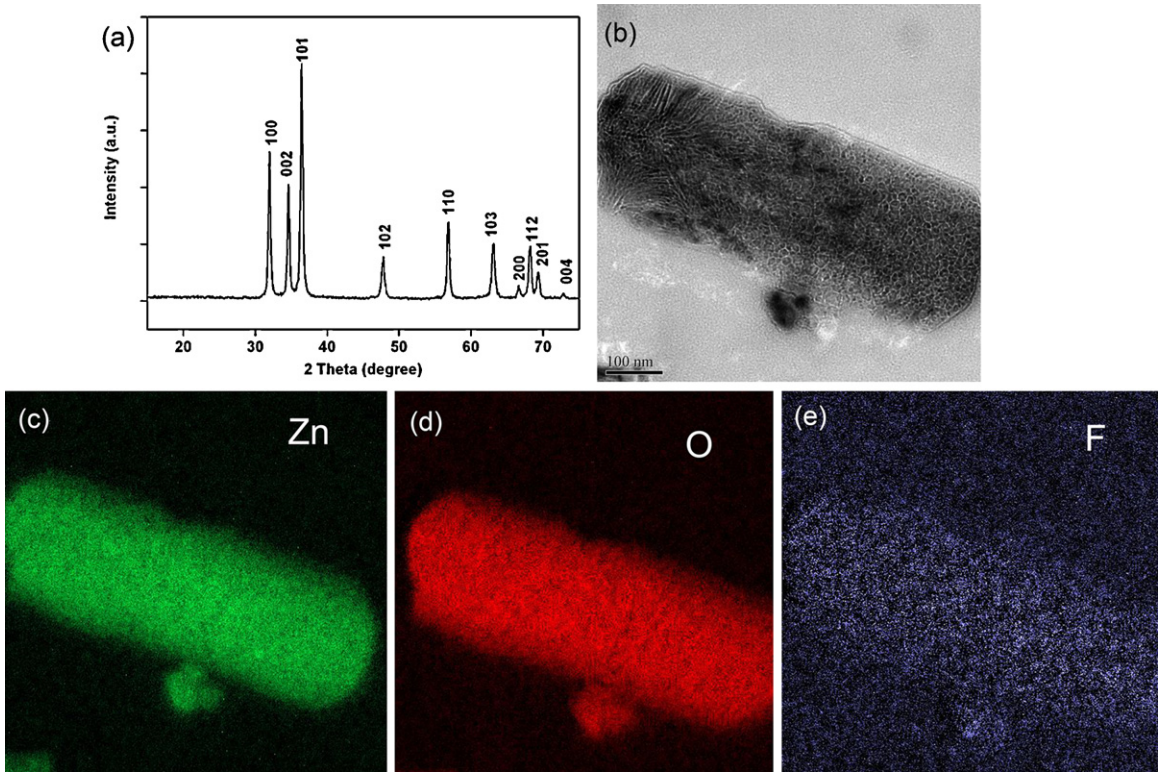

Fig. 2. (a) XRD pattern, (b) typical TEM image and X-ray elemental mapping results corresponding to (c) Zn, (d) O, and (e) F of the sample after annealing.

corresponding Fourier Transform (FFT) pattern from the whole area. Therefore, both the results of SAED and HRTEM indicate that these F-ZnO prisms are composed of highly oriented nanograins, which sets our novel hierarchically porous prisms apart from the typical polycrystalline porous ZnO rhombus-like NRs reported by Xu et al. [19].

The SEM and TEM images of the F-ZnO films indicate that ZnF(OH) prism films are used as "self-templates" for producing

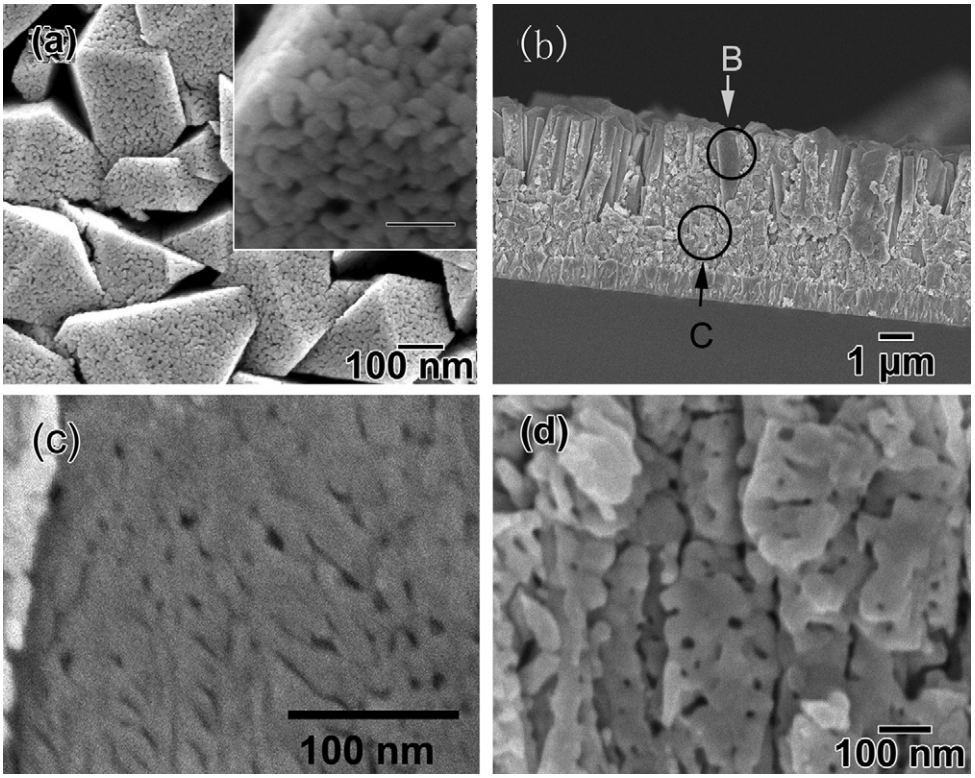

Fig. 3. (a) SEM image (inset: high magnification image) and (b) cross-sectional SEM image of the porous F-ZnO PA. (c) and (d) Enlarged SEM images corresponding to region B and region C in panel (b).

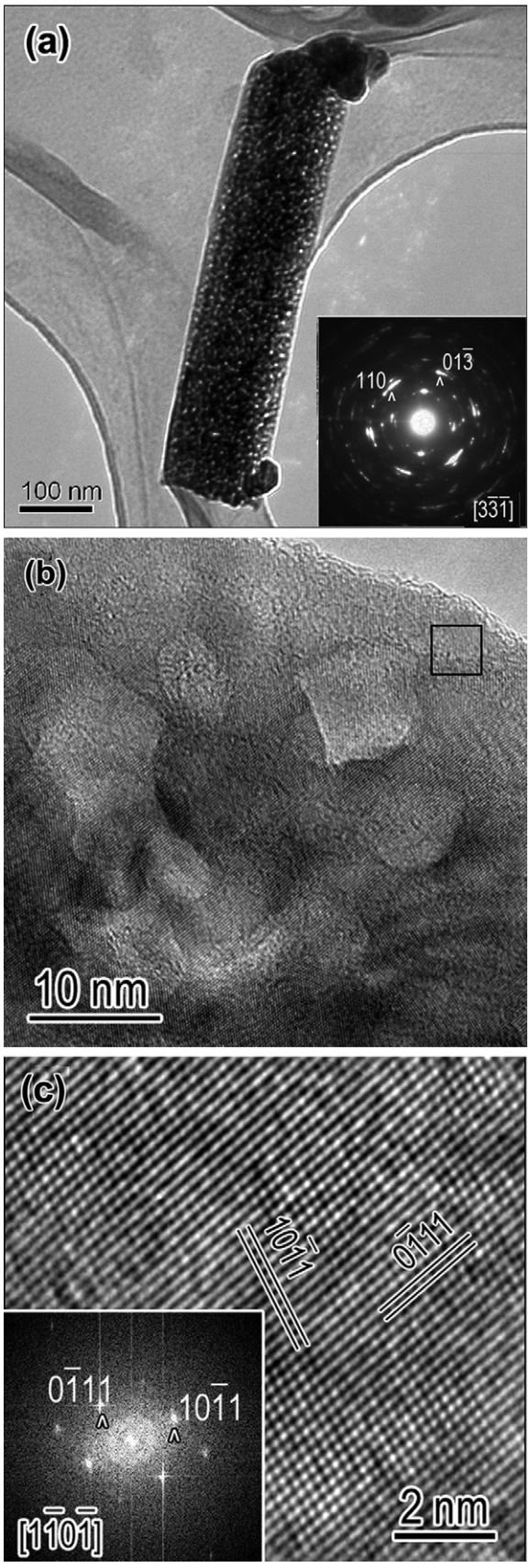

Fig. 4. (a) TEM image and corresponding SAED pattern (in the inset) of a single F-ZnO prism. (b) TEM image at high magnification. (c) HRTEM taken from the square in panel (b) and its corresponding FFT pattern from the whole area in (c).

F-ZnO films with similar morphology. Furthermore, F-ZnO PA films have a large surface area because each prism consists of nanoparticles and nanopores. Porous structure is necessary for the penetration of electrolyte into the photoanode. Thus the novel hierarchically porous PA films, which maintain the characteristic fast electron transport channels of vertically aligned NR, while offering enlarged surface area for dye adsorption, might significantly enhance the overall efficiency of the DSSCs.

3.3. Formation mechanism of the single-crystalline ZnF(OH) PA

During the process of ZnF(OH) precursor formation, NH_4F is used as a control agent to inhibit homogeneous precipitation of zinc hydroxide in solution and to make fluoride hydroxide deposit heterogeneously on the substrate [27]. Saito et al. [27] reported the heterogeneous nucleation and growth mechanism of ZnF(OH), and indicated the chemical reaction in the process could be formulated as follows:

A small amount of Zn^{2+} forms complexes with OH^-:

$$Zn^{2+} + nOH^- \Leftrightarrow Zn(OH)_n{}^{2-n} \quad (2)$$

Zn^{2+} ions form complexes with existing F^- ions:

$$Zn^{2+} + F^- \Leftrightarrow ZnF^+ \quad (3)$$

and zinc fluoride hydroxide precipitates through the reaction between ZnF^+ and OH^-:

$$ZnF^+ + OH^- \Leftrightarrow ZnF(OH)\downarrow \quad (4)$$

Moreover, Zn^{2+} forms amine complexes with NH_3 under high pH conditions:

$$Zn^{2+} + nNH_3 \Leftrightarrow Zn(NH_3)_n{}^{2+} \quad (5)$$

with $n = 1$–4, where NH_3 is in equilibrium with $NH_4{}^+$ and OH^- as

$$NH_4{}^+ + OH^- \Leftrightarrow NH_3 \quad (6)$$

In our case, during the nucleation stage, the newly produced ZnF(OH) nanoparticles are heterogeneously nucleated on the ZnO seed nanoparticles that were pre-dip-coated on the surface of FTO, because the energy barrier for this nucleation is lower than that for nucleation in solution. Then, oriented vertical growth occurs via attachment of ZnF(OH) nanoparticles, leading to the formation of prisms. The unique rhombus-like endplanes originate from the intrinsic crystalline habit of the orthorhombic crystals. To evaluate the influence of growth duration on the morphology of ZnF(OH), we have studied the time course of the reaction by SEM. Fig. S5 in the Supporting Information displays a series of images that show the morphological evolution of ZnF(OH) films reacted for different times (from 0 to 120 min). In Fig. S5a, the SEM image of the ZnO seed layer produced by dip-coating shows a large expanse of ZnO seed nanoparticles. After 5 min of reaction, thin NRs could be observed over the whole substrate as shown in Fig. S5b. As the reaction continued to 10 min, we can see that the prisms grew perpendicular to the substrate as shown in Fig. S5c. Increasing the growth time to 60 min leads to an increase of not only the prisms length, but also their width (Fig. S5d–S5e). Even though the width increases, no tapering of the prisms can be found. The distances across the prisms have a wide range, from 100 nm to 1.5 μm, resulting from the non-uniform distribution of the nanocrystalline ZnO seed layer. Such a polydispersed size distribution of prisms in the film is thought to promote effective light scattering. Further prolonging the growth time to 120 min results in the formation of ZnF(OH) prisms with micrometer size and near-disappearance of the spaces between the prisms as shown in Fig. S5f. This lengthy growth time led to the fusion of prisms with each other. The growth time is therefore crucial to obtain a thick ZnF(OH) film with this novel architecture.

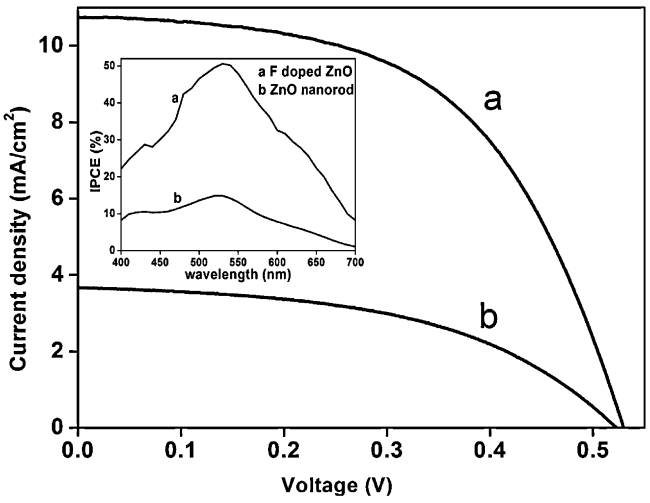

Fig. 5. *J–V* curves and IPCE curves (in the inset) of DSSCs based on F-ZnO PA and ZnO NR photoanodes.

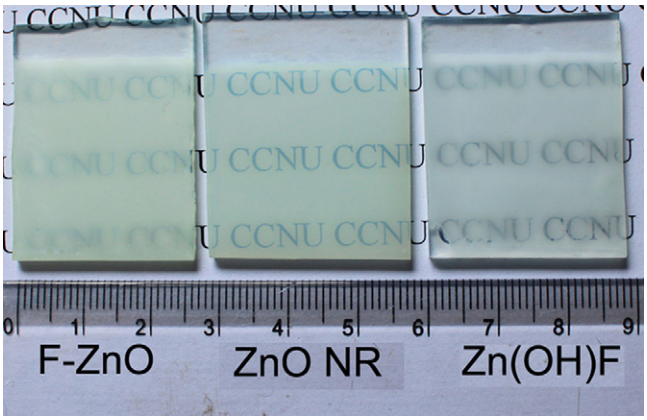

Fig. 6. Digital photograph of the 3-μm thick films with F-ZnO PA (left), ZnO NR (center) and ZnF(OH) PA (right).

3.4. Photovoltaic properties of the mesoporous F-ZnO PA base DSSCs

In a preliminary attempt, mesoporous F-ZnO PAs with a thickness of approximately 5 μm were fabricated for use as photoanodes in DSSC tests. For comparison, a hexagonal ZnO NR array (Fig. S6) photoanode with the same thickness was also constructed. Fig. 5 shows the characteristic photocurrent-voltage (*J-V*) curves with both curves under AM 1.5 sunlight illumination (90 mW cm^{-2}) and (in the inset) monochromatic incident photon-to-current conversion efficiency (IPCE), and their photovoltaic parameters derived from the *J–V* curves are summarized in Table 1. An overall solar to electrical energy conversion efficiency (η) of 3.43% was achieved for F-ZnO PA DSSC with a current density (J_{sc}) of 10.75 mA cm^{-2}, open-circuit voltage (V_{OC}) of 0.53 V, and fill factor (*FF*) of 54%, much higher than the performance of the ZnO NR array based DSSC (η = 1.04%, J_{sc} = 3.66 mA cm^{-2}, V_{OC} = 0.52 V, *FF* = 48%). This efficiency (3.43%) is attractive, taking into account that the film thickness is only 5 μm. The improvement in η value of the F-ZnO PA DSSC is obviously caused by the higher J_{sc}. Moreover, the IPCE values obtained for the F-ZnO PA DSSC are higher than those of the ZnO NR DSSC in the visible-wavelength. The evidence of the improvement in the IPCE values further confirms the higher J_{sc} for the F-ZnO PA DSSC as compared with the ZnO NR DSSC. The enhanced photocurrent could be attributed to the enhanced light harvesting due to the better dye adsorption, enhanced light reflection and scattering of the photoanode, as well as improved charge collection due to increased electron lifetime, which will be discussed below. The slightly higher V_{OC} of F-ZnO PA DSSC should be a result of the addition of the F into the ZnO to decrease charge recombination [28].

The amount of adsorbed dye was measured by desorbing the N719 dye into 0.2 mM NaOH solution and analyzing the solution using the adsorption peak intensity of N719 at 501 nm, and the results are also presented in Table 1. The dye loading was calculated to be 1.47×10^{-4} mM and 8.91×10^{-5} mM for the F-ZnO PA and the ZnO NR array, respectively (both anodes were 1.68 cm^2 in area and 3 μm thick). Since the amount of dye absorbed on the F-ZnO PA DSSC is 1.7 times more than that on ZnO NR DSSC, some of the improved photocurrent for the F-ZnO PA DSSC is because of its mesoporous structure, which provides increased effective surface area for dye adsorption.

The size and morphology of 1D ZnO have been demonstrated to play important roles in controlling the light scattering [29]. Furthermore, it has been reported that dense nanocavities could significantly enhance the optical absorption coefficient of TiO_2 [30]. The enhanced light scattering of ZnO photoanode films is important for improving the light-harvesting efficiency, and this has attracted much interest in developing mesoporous hierarchical structures to boost photon-to-current conversion efficiency of DSSCs [31,32]. Fig. 6 shows digital photographs of three FTO substrates coated with F-ZnO PA (left), ZnO NR film (center) and ZnF(OH) PA (right) with the same thickness (3 μm). After thermal treatment, the F-ZnO PA substrate became more opaque than that of ZnF(OH) PA, while the ZnO NR coated substrate is nearly transparent. The opacity of the F-ZnO PA substrate is due to the stronger light scattering by the mesoporous prisms as compared with the ZnO NRs. The polydispersity of the prisms' width (100 nm to 1.5 μm) [33] and the presence of the mesopores are particularly desirable for enhanced light scattering and trapping.

To further investigate the F-doping effect on the electron-injection process in the N719 dye sensitized F-ZnO PA (F-ZnO/N719) structure, green PL measurements of F-ZnO/N719 film and ZnO NR/N719 film were carried out (Fig. S7 in the supporting information). Both of the samples show a band at 550 nm corresponding to N719 molecules [34], while the emission from the F-ZnO/N719 film is completely quenched. The complete quenching PL behavior of F-ZnO/N719 suggests efficient separation of holes and electrons, which is critical for fast electron injection, and consequently enhancement of photovoltaic performance of the F-ZnO PA DSSC.

The EIS spectra of the two DSSCs based on the F-ZnO PA film and ZnO NR film under illumination were measured ranging from 0.1 Hz to 100 kHz at the V_{OC} with values of 0.53 V and 0.52 V, respectively, as illustrated in Fig. 7. According to the diffusion-recombination model [35,36], a suggested equivalent circuit representing the processes of electron transport and recombination are shown in Fig. 7a. Fig. 7b shows the corresponding Nyquist plots of the F-ZnO PA DSSC and ZnO NR DSSC, respectively. The semicircles in the high-frequency region are related to the charge-transfer process at the electrolyte/counter electrode interface with the resistance (R_{pt}) and C_{pt} in parallel. In the low frequency the large arcs are assigned to the electron transport resistance, R_w, and the charge-transfer resistance related to recombination of electron at the ZnO/electrolyte interface, R_k. As shown in Fig. 7b, there is a big difference in the low frequency region for the tow DSSCs. In the case of F-ZnO PA DSSC, there is much higher internal surface area of F-ZnO PA electrode for sufficient dye adsorption and light harvesting efficiency. Thus under illumination, the photogenerated electron density of F-ZnO PA is remarkable higher than that of ZnO NR resulting in an increase in the electron density which leads to both small R_k and R_w in the case of F-ZnO PA. As we all know, efficiency of

Table 1
Photovoltaic parameters of the F-ZnO PA and ZnO NR based DSSCs under AM 1.5 sunlight illumination (90 mW cm^{-2}).

Sample	J_{SC} (mA cm^{-2})	V_{OC} (V)	*FF*	Efficiency (%)	Dye adsorbed (mM)
F-ZnO PA	10.75	0.53	0.54	3.43	1.47×10^{-4}
ZnO NR	3.66	0.52	0.48	1.04	8.91×10^{-5}

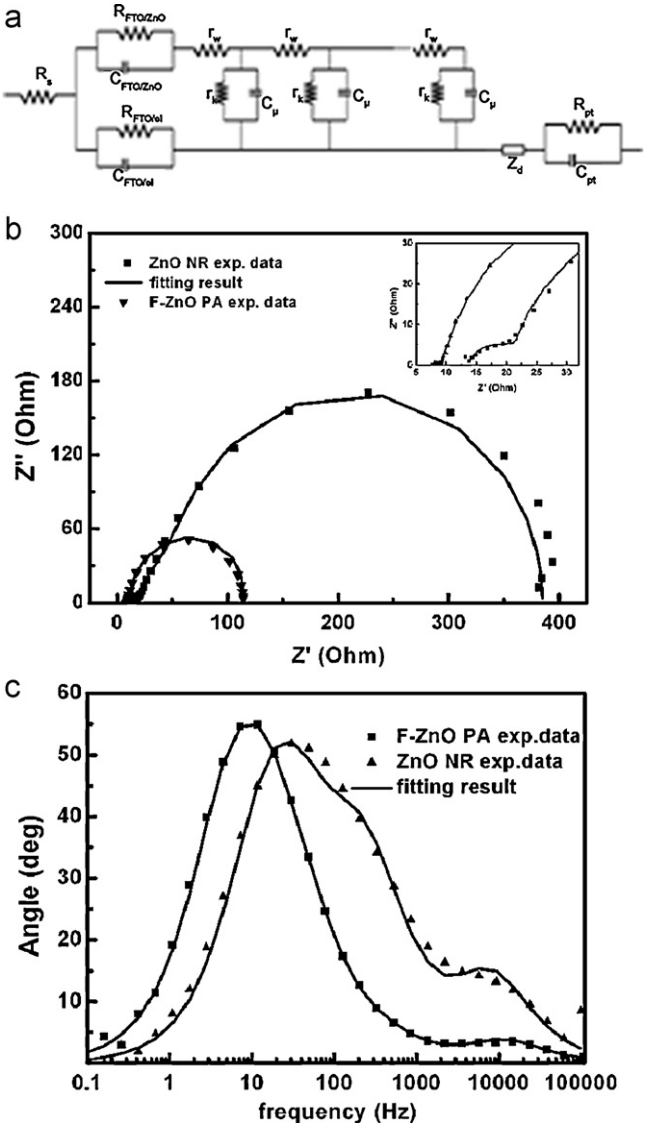

Fig. 7. (a) Equivalent circuit model. R_w is electron transport resistance in the ZnO film; R_k is the charge transfer resistance related to recombination at ZnO/electrolyte interface; c_μ is the chemical capacitance in ZnO film; Z_d is the Nernst diffusion impedance; R_{Pt} and C_{Pt} are the charge transfer resistance and capacitance at the Pt/electrolyte interface, respectively; R_{FTO}/ZnO and C_{FTO}/ZnO are the resistance and capacitance at the contact between ZnO and FTO, respectively; R_{FTO}/el and C_{FTO}/el are the charge transfer resistance and capacitance at the FTO/electrolyte interface on the photoanode side, respectively; R_s is the sheet resistance. (b) Nyquist and (c) bode plots of the impedance data of the F-ZnO PA and ZnO NR DSSCs. The solid lines are the fitting results based on the equivalent circuit model, respectively.

photogenerated electron collection is determined by the competition between transport of electron in the electrode and recombination. As a result, the electrons for transport and recombination in the F-ZnO PA electrode both increased, compared to ZnO NR electrode. Above all, despite the increased charge recombination, there are more photogenerated electrons for F-ZnO PA than that of ZnO NR tranferring to the external circuit all the same. In addition, from the Bode plot in Fig. 7c, the low-frequency peak apparently shifts to a lower frequency, corresponding to an increase in the electron lifetime (τ) for F-ZnO DSSCs. The electron lifetime (τ) can be extracted from the frequency (f_{max}) at the low-frequency peak in the Bode-phase plots using $\tau = 1/2\pi f_{max}$. A much longer τ was found in the case of the cell with porous F-ZnO (13.6 ms) than for the cell with ZnO NR (5 ms). The increased τ could be attributed to the F dopant, which acts as a charge trapping site for electron–hole separation. The longer electron lifetime will also favor electron transport over a longer distance with less diffusive hindrance to some extent, and thus lead to the reduction of electron combination and the capture of more effective electrons [37,38]. Therefore, the porous F-ZnO PA based DSSCs exhibit better performance than the ZnO NR based DSSCs.

4. Conclusion

In summary, we successfully prepared a superstructure of mesoporous F-ZnO PA with highly oriented crystal grains by pyrolysis of a ZnF(OH) PA precursor in air. The decomposition of the precursor and the release of gases resulted in a large amount of nanopores among the prisms. The preparation procedures for mesoporous F-ZnO PA film are simple, reproducible, and easy to scale up at low cost. A 5 μm thick F-ZnO PA photoanode based DSSC showed a solar to electrical energy conversion efficiency (η) of 3.43%, while the efficiency of a cell with ZnO NR photoanode was 1.04%. The superior performance of the DSSC with porous F-ZnO PAs, relative to that of the DSSC with ZnO NRs, is attributed to the higher IPCE, higher surface area, stronger light scattering, as well as longer electron lifetime. This achievement is remarkable, as the DSSC parameters reported here are far from being optimized. Further experiments are under way to investigate the effect of the fundamental geometrical features of F-ZnO PAs on solar cell conversion efficiency, to deduce the most promising strategies for improvement.

Supporting information

TG–DTA curves of the Zn(OH)F precursors; XPS spectrum, UV–vis absorption spectra and PL spectrum of the F-ZnO PA; SEM image and green PL spectrum.

Acknowledgment

Financially supported by self-determined CCNU basic research and operation research funds for colleges from the China Ministry of Education (CCNU09A02011).

Appendix A. Supplementary data

Supplementary data associated with this article can be found, in the online version, at doi:10.1016/j.jpowsour.2011.08.011.

References

[1] C. Nauer, G. Boschloo, E. Mukhtar, A. Hagfeldt, J. Phys. Chem. B 105 (2001) 5585.
[2] E. Hosono, Y. Mitsui, H. Zhou, Dalton Trans. (2008) 5439.
[3] L. Schmidt-Mende, J.L. MacManus-Driscoll, Mater. Today 10 (2007) 40.
[4] W.I. Park, G.C. Yi, M. Kim, S.J. Pennycook, Adv. Mater. 14 (2002) 1841.
[5] L.E. Greene, M. Law, K.H. Tan, M. Montano, J. Goldberger, G. Somorjai, P. Yang, Nano Lett. 5 (2005) 1231.
[6] E. Guillen, E. Azaceta, L.M. Peter, A. Zukal, R. Tena-Zaera, J.A. Anta, Energy Environ. Sci. (2011), doi:10.1039/c0ee00500b.

[7] A. Cheng, Y. Tzeng, Y. Zhou, M. Park, T. Wu, C. Shannon, D. Wang, W. Lee, Appl. Phys. Lett. 92 (2008) 092113.
[8] R.A. Jensen, H. Ryswyk, C. She, J. Szarko, L. Chen, J. Hupp, Langmuir 26 (2010) 1401.
[9] Q. Zhang, C. Dandeneau, X. Zhou, G. Cao, Adv. Mater. 21 (2009) 4087.
[10] M. Guo, P. Diao, S. Cai, Chin. Chem. Lett. 15 (2004) 1113.
[11] Y. Qiu, W. Chen, S.J. Yang, Mater. Chem. 20 (2010) 1001.
[12] Q. Zhang, T. Chou, B. Russo, S. Jenekhe, G. Cao, Angew. Chem. Int. Ed. 47 (2008) 2402.
[13] Y. Shi, C. Zhan, L. Wang, B. Ma, R. Gao, Y. Zhu, Y. Qiu, Adv. Funct. Mater. 20 (2010) 437.
[14] Y. Zheng, X. Tao, Q. Hou, D. Wang, W. Zhou, J. Chen, Chem. Mater. 23 (2011) 3–5.
[15] A. Gonçalves, M.R. Davolos, N. Masaki, S. Yanagida, A. Morandeira, J.R. Durrant, J.N. Freitas, A.F. Nogueira, Dalton Trans. (2008) 1487.
[16] S. Kim, Y. Kim, J. Choi, J. Cryst. Growth 312 (2010) 2946–2951.
[17] N. Audebrand, J.-P. Auffrèdic, D. Louër, Chem. Mater. 10 (1998) 2450.
[18] E. Hosono, S. Fujihara, T. Kimura, I. Honma, H. Zhou, Adv. Mater. 17 (2005) 2091–2094.
[19] F. Xu, L. Sun, M. Dai, Y. Lu, J. Phys. Chem. C 114 (2010) 15377–15382.
[20] D. Raviendra, J.K. Sharma, J. Appl. Phys. 58 (1985) 838.
[21] Y.W. Tang, X.Y. Hu, M.J. Chen, L.J. Luo, B.H. Li, L.Z. Zhang, Electrochim. Acta 54 (2009) 2742.
[22] F. Xu, M. Dai, Y.N. Lu, L.T. Sun, J. Phys. Chem. C 114 (2010) 2776.
[23] P.M. Ratheesh Kumar, C. Sudha Kartha, K.P. Vijayakumar, F. Singh, D.K. Avasthi, Mater. Sci. Eng. B 117 (2005) 307–312.
[24] A. Khan, M. Kordesch, Mater. Lett. 62 (2008) 230.
[25] A. Khan, W.M. Jadwisienczak, M. Kordesch, Physica E 33 (2006) 331.
[26] A. Guillén-Santiago, M. de la, L. Olvera, A. Maldonado, R. Asomoza, D.R. Acosta, Phys. Status Solidi A 201 (2004) 952.
[27] N. Saito, H. Haneda, W. Seo, K. Koumoto, Langmuir 17 (2001) 1461–1469.
[28] H. Tian, L. Hu, C. Zhang, W. Liu, Y. Huang, L. Mo, L. Guo, J. Sheng, S. Dai, J. Phys. Chem. C 114 (2010) 1627.
[29] J. Elias, C. Lévy-Clément, M. Bechelany, J. Michler, G. Wang, Z. Wang, L. Philippe, Adv. Mater. 22 (2010) 1607–1612.
[30] W. Han, L. Wu, R. Obert, F. Klie, Y. Zhu, Adv. Mater. 19 (2007) 2525.
[31] D. Chen, F. Huang, Y. Cheng, R.A. Caruso, Adv. Mater. 21 (2009) 2206.
[32] H. Li, Z. Bian, J. Zhu, D. Zhang, G. Li, Y. Huo, H. Li, Y. Lu, J. Am. Chem. Soc. 129 (2007) 8406.
[33] R. Tena-Zaera, J. Elias, C. Lévy-Clément, Appl. Phys. Lett. 93 (2008) 233119.
[34] A. Du Pasquier, H. Chen, Y. Lu, Appl. Phys. Lett. 89 (2006) 253513.
[35] J. Bisquert, J. Phys. Chem. B 106 (2002) 325.
[36] M. Adachi, M. Sakamoto, J. Jiu, Y. Ogata, S. Isoda, J. Phys. Chem. B 110 (2006) 13872.
[37] E.S. Kwak, W. Lee, N.G. Park, J.H. Kim, H. Lee, Adv. Funct. Mater. 19 (2009) 1093.
[38] C. He, Z. Zheng, H. Tang, L. Zhao, F. Lu, J. Phys. Chem. C 113 (2009) 10322.